# Structure-based prediction of Wnt binding affinities for Frizzled-type cysteine-rich domains

**Mark Agostino[1,2], Sebastian Öther-Gee Pohl[1], Arun Dharmarajan[1]**

[1]Stem Cell and Cancer Biology Laboratory, School of Biomedical Sciences and Curtin Health Innovation Research Institute, Curtin University, Kent St, Bentley WA 6102, Australia
[2]Curtin Institute of Computation, Curtin University, Kent St, Bentley WA 6102, Australia

To whom correspondence should be addressed to: Dr Mark Agostino, Stem Cell and Cancer Biology Laboratory, School of Biomedical Sciences, Curtin Health Innovation Research Institute and Curtin Institute of Computation, Curtin University, Kent St, Bentley WA 6102, Australia. Phone: +61892669719. E-mail: Mark.Agostino@curtin.edu.au.

Keywords: Wnt signaling, Frizzled receptor, cysteine-rich domain, structure-activity relationship, homology modeling, structural biology, protein-protein interaction, lipid-protein interaction

## ABSTRACT

**Wnt signaling pathways are of significant interest in development and oncogenesis. The first step in these pathways typically involves the binding of a Wnt protein to the cysteine-rich domain (CRD) of a Frizzled receptor; Wnt-Frizzled interactions can be antagonized by secreted Frizzled-related proteins (sFRPs), which also contain a Frizzled-like CRD. The large number of Wnts, Frizzleds and sFRPs, as well as the hydrophobic nature of Wnt, pose challenges to laboratory-based investigations of interactions involving Wnt. Here, utilizing structural knowledge of a representative Wnt-Frizzled CRD interaction, as well as experimentally-determined binding affinities for a selection of Wnt-Frizzled CRD interactions, we generate homology models of Wnt-Frizzled CRD interactions and develop a quantitative structure-activity relationship for predicting their binding affinities. The derived model incorporates a small selection of terms derived from scoring functions used in protein-protein docking, as well as an energetic term considering the contribution made by the lipid of Wnt to the Wnt-Frizzled binding affinity. Validation with an external test set suggests that the model can accurately predict binding affinity for 75% of cases, and that the error associated with the predictions is comparable to the experimental error. The model was applied to predict the binding affinities of the full range of mouse and human Wnt-Frizzled and Wnt-sFRP interactions, indicating trends in Wnt binding affinity for Frizzled and sFRP CRDs. The comprehensive predictions made in this study provide the basis for laboratory-based studies of previously unexplored Wnt-Frizzled and Wnt-sFRP interactions, which in turn, may reveal further Wnt signaling pathways.**

The Wnt signaling pathway is an evolutionary conserved pathway found in vertebrates and insects (1). It functions to regulate body axis formation, cell fate, cell proliferation and morphogenesis in embryonic development (2), while aberrant Wnt signaling is a hallmark of many cancers (3). Wnt signaling pathways can be divided into three separate branches, a canonical, or β-catenin dependent pathway, and two non-canonical or β-catenin independent pathways, known as the planar cell polarity (PCP) and Wnt/$Ca^{2+}$ pathways (4,5) (Figure 1). Wnt signaling is generally initiated by the binding of Wnt ligands binding to a Frizzled (Fzd) receptor (6). In the canonical Wnt signaling pathway (Figure 1a), low-density-lipoprotein-related protein 5/6 (LRP5/6) acts as a co-receptor for Wnt binding (7). Signal transduction by the three major Wnt signaling pathways is regulated by the interaction of Fzd with the cytoplasmic protein Dishevelled (Dvl) (8). In the canonical pathway, β-catenin dependent signaling is mediated through the cytoplasmic 'destruction complex' composed of Axin, protein phosphatase 2A (PP2A), adenomatous polyposis coli protein (APC), glycogen synthase kinase 3 (GSK3) and casein kinase 1α (CK1α) (9). In the presence of Wnt stimulation, Fzd is activated, permitting Dvl binding, and resulting in the stabilization of the destruction complex and the accumulation of non-phosphorylated β-catenin, which then translocates to the nucleus and binds to TCF/LEF transcription factors on the promoter of target genes (4). In the absence of Wnt stimulation, the

destruction complex is destabilized, allowing for the phosphorylation of β-catenin by CK1α and GSK3 (10); phosphorylated β-catenin is then proteolytically degraded (11). The Wnt/$Ca^{2+}$ pathway (Figure 1b) is activated through Wnt ligands binding to Fzd receptors, resulting in an increase in intracellular calcium (12). Calcium ions are able to activate both calmodulin-dependent protein kinase II (CaMKII) (13) and protein kinase C (PKC) (14), which subsequently activate transcription factors NFκB and CREB. The cytosolic phosphatase, calcinurin (Cn), is also activated by calcium ions. Cn-dependent dephosphorylation, and activation of NFAT, leads to the transcription of genes in cardiomyocytes, neuronal cells and skeletal muscle (15). Signal transduction via the PCP pathway (Figure 1c) is initiated through Wnt binding to Fzd and co-receptors receptor tyrosine kinase-like receptor ROR and Ryk. Fzd activation leads to Dvl-mediated activation of Rac and Rho. JNK and Rho kinase (ROCK) are activated by Rac and Rho, respectively which mediates actin polymerization and activates transcription factors AP-1 and JUN (16).

Wnts comprise a group of 19 proteins that are subject to numerous post-translational modifications, including the formation of a large number of characteristic disulfide bonds, glycosylation in the endoplasmic reticulum (17), and palmitoleylation by Porcupine, which aids in their secretion and facilitates their interaction with Frizzled (18). Structurally, as determined by the co-crystallization of *Xenopus* Wnt8 (XWnt8) with the mouse Fzd8 CRD, Wnts are composed of two domains: an amino-terminal (NTD) and carboxy-terminal domain (CTD) (19). The NTD contains 10 cysteine residues forming 5 disulfide bridges, in a cluster of α-helices, while the CTD contains 6 disulfide bridges and a two-stranded β-sheet (19). Frizzled receptors are a group of ten membrane-bound receptors comprising the majority of Class F G-coupled protein receptors (GPCRs). Frizzleds, like other GPCRs, consist of seven hydrophobic transmembrane helices, but feature an extracellular cysteine-rich domain (CRD) in their N-terminal (20). The CRD is characterized by a conserved pattern of ten cysteines, and can bind Wnt and Norrin ligands (21,22). The five mammalian secreted frizzled related proteins (sFRPs) are secreted glycoproteins, composed of an N-terminal CRD located and a C-terminal netrin-like domain (NLD) (23). These proteins function to antagonize the Wnt signaling pathway (24) through binding of either the CRD (25) or the NLD to Wnt ligands (26), thus interfering with Wnt binding to Fzd and preventing β-catenin-mediated gene transcription. The sFRPs have been studied in great detail for their potential roles as tumor suppressors and their implications in carcinogenesis (23).

Due to the large number of possible Wnt-Fzd CRD interactions (which, considering CRDs from both Fzds and sFRPs, totals 285 interactions per species), it is challenging to investigate these experimentally. A recent study utilized biolayer interferometry (BLI) to investigate a small set of mouse Wnt-Fzd CRD interactions in a combinatorial manner (27). Numerous other interactions have been identified via co-immunoprecipitation (coIP), or proposed based on co-expression of particular Wnts with particular Fzds (6). While coIP and co-expression are valuable methods for suggesting the existence of specific protein-protein interactions, they are unable to provide an indication of the likely strength of an interaction. Computational studies provide the opportunity to complete the knowledge of interactions between Wnts and Fzd CRDs, and may reveal previously unexplored high affinity interactions.

In this study, we have generated homology models of Wnt complexes with both Fzd and sFRP CRDs and predict the likely binding affinity associated with these interactions. For a series of Wnt-Fzd CRD interactions for which dissociation constants have been reported (27), we then evaluated the interaction energy for the protein-protein and lipid-protein components of the interactions; this was achieved through scoring the interactions against the full set of functions contained in CCharPPI (28) (for the protein-protein component) and scoring using Prime MM-GB/SA (for the lipid-protein component). Strike was then used to develop and evaluate binding affinity prediction models, using scores obtained from CCharPPI and Prime MM-GB/SA as descriptors for the model building. A model with high predictive performance was identified, and subsequently applied to predict the binding affinities of all Wnt-Fzd and Wnt-sFRP CRD interactions, in both mouse and human cases.

## RESULTS

*Preparation of homology models of Wnt-Fzd CRD complexes*–We prepared homology models of all mouse and human Wnts, and all

mouse and human Fzd and sFRP CRDs; details of UniProt accession numbers, sequence ranges and sequence alignments used to build the models are provided in the Supplemental Data (Table S1, Figures S2 and S3). The vast majority of proteins modelled did not feature large insertions or deletions relative to either XWnt8 or mFzd8 CRD, with the exceptions of mouse and human Wnt6, Wnt10a and Wnt10b; these Wnts feature insertions relative to XWnt8 larger than that able to be built by Prime (greater than twenty residues). To build these structures, we utilized an alternative procedure incorporating the I-TASSER server (described in detail in the Experimental Procedures), which is capable of building much longer insertions than Prime through its use of an iterative template fragment assembly approach to model building (29).

Following assembly of the complexes and refinement using procedure automated using KNIME (Figure S4), the MolProbity score of all models was calculated. The MolProbity score provides a single value metric of structural quality, summarizing the number of atomic clashes, percentage of backbone conformations in regions outside the Ramachandran favored regions, and the percentage of bad side-chain rotamers (30). The TM-score and the root-mean-squared deviation (RMSD) of the Cα atoms of the models with respect to the XWnt8-mFzd8 CRD complex structure (PDB 4F0A) (19), which was the template for all models, were also calculated. These measures assess differences in the co-ordinates of two structures (31). The mean value for the MolProbity scores for the mouse and human models was slightly greater than the MolProbity score obtained for the XWnt8-mFzd8 CRD complex structure (Table 1) but nonetheless comparable, indicating the generally high quality of the models. The mean values for the model TM-Scores with respect to the template crystal structure were generally high and the mean values for the model Cα RMSDs very low, further indicating the generally high quality of the models and their limited divergence from the template crystal structure. Selected complexes are shown in Figure 2. Quality metrics are summarized in Table 1, and full details are provided in the Supplemental Data (Tables S5-S10).

*Development and validation of a Wnt-Fzd CRD binding affinity prediction model*–We used a set of mouse Wnt-Fzd CRD binding affinities determined by BLI (27) to develop and validate our binding affinity prediction model. The model building and evaluation procedure is summarized in Figure 3, and herein described.

Within the BLI data, we designated a *training* set, used to optimize the model, and a *test* set, used to demonstrate the performance of the model for data against which it had not been trained. Our training set was designated as complexes that were not part of our test set; our test set consisted of complexes involving interactions with either mFzd4 or mWnt1. The definition of the test set in this manner provided a simple means of selecting a test set covering a wide range of affinities. For all of these complexes, we then rescored, with separate procedures, the protein-protein portion and the lipid-protein portion of the interaction. The protein-protein portion was rescored against the majority of functions available within CCharPPI (28) (detailed in Table S11), a server compiling a wide range of scoring functions suitable for use in protein-protein docking. The lipid-protein portion was rescored used Prime MM-GB/SA, which provides a rapid means for evaluating ligand-receptor binding energies with improved accuracy compared to typical docking scoring functions. The Prime MM-GB/SA calculation is also decomposed into its components (Coulomb/electrostatic, covalent binding, van der Waals, lipophilic, polar solvation/desolvation, hydrogen bonding and π-π components; components used in this study detailed in Table S11). The two strategies function complementarily to one another; the functions in CCharPPI are only capable of considering interactions between standard protein amino acids, while Prime MM-GB/SA is only capable of studying interactions between small organic molecules with proteins. With this in mind, the Wnt lipid was removed from the CCharPPI calculations, and the Wnt protein was removed from the Prime MM-GB/SA calculations (that is, only the interaction between the Wnt lipid and the Fzd CRD was assessed by Prime MM-GB/SA). Multiple linear regression models combining one Prime MM-GB/SA component with one or more CCharPPI components (all herein referred to as *descriptors*) were then generated, thus allowing the development of a single model considering both the protein-lipid and the protein-protein portions of the interaction.

As it was computationally accessible to consider all possible three-descriptor models incorporating one Prime MM-GB/SA term and two CCharPPI-derived terms, we initially

explored these. The performance of all models was evaluated using two principle metrics:

1) The root-mean-square error (RMSE) between the predicted values and the average experimental values ($RMSE_{train}$, $RMSE_{test}$); lower values indicate a better fit between the predictions and experimental values
2) The percentage of complexes for which the predicted value occurred within the experimental range reported ($InExp_{train}$, $InExp_{test}$); higher values indicate a better fit between the predictions and experimental values

High performing three-descriptor models of Wnt-Fzd CRD binding typically incorporated the van der Waals term of the Prime MM-GB/SA calculation (Table S12). The lipophilic term of the Prime MM-GB/SA calculation also appears frequently in high performing models. This is unsurprising considering the physicochemical properties of palmitoleic acid, which would suggest that the binding energy will likely be associated with van der Waals/non-polar interactions. The best performing three-descriptor models generally displayed root-mean-squared errors (RMSEs) for both the training and test sets in the range of 0.3-0.4 kcal/mol, well outside the error range of the experiments of approximately 0.2-0.3 kcal/mol (27); this indicates that three-descriptor models are insufficiently predictive.

Two models containing four descriptors were identified that were capable of high prediction performance (Table 2). Both of these displayed RMSEs for the training and test sets less than 0.3 kcal/mol. Both included the van der Waals term of the Prime MM-GB/SA calculation, the PyRosetta hydrogen bonding potential (HBOND2) (32) and either the RW or RWplus statistical potentials (AP_calRW, AP_calRWp) (33). The fourth term in Model 1 is the antibody-antigen energy function of FireDock (FIREDOCK_AB) (34), while in Model 2, it is the total RosettaDock weighted energy (ROSETTADOCK). As the performance of Model 1 appeared slightly improved over Model 2, this model was selected for further study. Additionally, Model 1 was preferred over Model 2 for featuring a smaller constant term, suggesting that it may be able to predict affinities over a wider range than Model 2. The RMSE values for Model 1 suggest that the error associated with its use will be slightly larger than, but nonetheless similar to, the error range achieved by experiment.

The maximum difference between any prediction made by the model, either in the training set or the test set, is approximately 0.6 kcal/mol, which corresponds to a difference in $K_d$ of approximately one order of magnitude (Figure 4, Table 3). Since there appears to be no particular Wnts or Fzds for which poor predictions are made, failure to make accurate predictions most likely occurs randomly and is not associated with a particular Wnt or Fzd structure; this is perhaps expected, given the overall high structural quality of the models used. The binding affinities of the vast majority of cases in the training and test sets are predicted within 0.25 kcal/mol of the mean experimental values reported, which is within the experimental error range.

Further elaboration of the selected four-descriptor models into five-descriptor models was performed, but did not result in models providing significant improvements in predictions (data not shown); similar RMSEs and a similar number of predictions occurring within the experimental ranges in both the training and test sets were obtained for the best four- and five-descriptor models. Thus, four-descriptor models were deemed sufficient for use in predicting binding affinities.

*Prediction of binding affinities of Wnt-CRD interactions*–In applying Model 1 to predict Wnt-CRD binding affinities in the mouse proteins, numerous trends are apparent (Figure 5A, Table S13). Fzd3, Fzd5, sFRP3 and sFRP4 generally display high affinity, non-specific binding of Wnts, as evidenced by more than half of the interactions predicted to afford strong binding affinities (i.e., <10nM). Fzd8 also displays non-specific binding of Wnts; however, the majority of interactions are predicted to be of lower affinity than those with Fzd3, Fzd5, sFRP3 and sFRP4. Fzd1, Fzd4, Fzd7 and Fzd9 generally display moderate affinity for a wide variety of Wnts. Fzd1, Fzd7 and Fzd9 display high affinity for limited Wnts, indicating more selective binding compared to Fzd3, Fzd5, Fzd8, sFRP3 and sFRP4, while Fzd4 displays high affinity for several Wnts, indicating less selective binding. Fzd1 displays high affinity for Wnt6, Fzd7 displays high affinity for Wnt10a, and Fzd9 displays high affinity for both Wnt7a and Wnt16. Fzd2, Fzd6, Fzd10, sFRP1, sFRP2 and sFRP5 all display moderate to high affinity binding to less than half of the Wnts. However, this does not strictly translate to high selectivity; Fzd6 and

Fzd10 bind with moderate affinity to several Wnts. Fzd2 displays high affinity for Wnt3a, Wnt7b and Wnt10a. sFRP1, sFRP2 and sFRP5 all display high selectivity for specific Wnt ligands, however, retain moderate affinity for the majority of remaining Wnts. sFRP1 appears highly selective for Wnt7a, while sFRP2 is selective for Wnt2b and Wnt3a. sFRP5 displays moderate affinity for Wnt2b, Wnt5b and Wnt6.

The human data generally displays similar trends to the mouse data (Figure 5B, Table S14). Fzd3, Fzd5, sFRP3 and sFRP4 still display generally high affinity, non-specific binding of Wnts, however, there are some specific points of difference. The interactions of human Fzd3 with Wnt8a and Wnt9a are predicted to be much higher affinity than in the case of the mouse, although the hFzd9:hWnt9a interaction is still predicted to be of only moderate affinity. Conversely, the interaction of human Fzd3 with Wnt5b is predicted to be of much lower affinity than the equivalent mouse interaction. The affinity of the mouse Wnt2 for sFRP3 and sFRP4 is predicted to be lower than the equivalent interactions in humans, however, Wnt9a is predicted to have increased affinity for these proteins in mouse compared to human. Significant differences in the predicted affinities of human Fzd4 for Wnt1, Wnt5a and Wnt11 compared to the mouse interactions are observed, with all of these interactions predicted to be very low in binding affinity in humans, whereas in mice these are all predicted to be very high affinity. Large differences in the predicted affinities occur when comparing the interactions of mouse and human Fzd6, Fzd10, sFRP1, sFRP2 and sFRP5 (Figure 5C); however, these interactions are generally predicted to be of low to moderate affinity and may not be indicative of different roles for Wnt interactions with these proteins in the two species.

*Analysis of residues of functional importance to Wnt-Fzd CRD interactions–*

To propose residues of functional importance to Wnt-Fzd interactions, all 570 Wnt-Fzd CRD models were subject to MM-GB/SA analysis with per-residue decomposition using AMBER14 (35). This calculation allows the identification of specific residues making large contributions to the binding energy, which in turn, can be used to suggest the most significant intermolecular contacts in the interaction. High affinity complexes will generally have more residues making large contributions to the binding energy compared to low affinity complexes; thus, high affinity complexes will have greater influence on the designation of sequence positions of general importance to Wnt-Fzd CRD interactions.

Analysis of Fzd CRD-binding regions of Wnt indicates two major regions utilized by Wnt in binding Fzd CRD (Figure 6A). These correspond to the thumb and index finger regions of Wnt, which are already well known as Fzd CRD-binding regions (19,36). Interestingly, Wnt residues beyond these two regions are rarely implicated in Fzd CRD binding (Figure S15) and the majority of Wnt residues in these regions frequently implicated in Fzd CRD binding are highly (often entirely) conserved in human and mouse Wnts.

In contrast to the Fzd CRD-binding regions of Wnt, which appear highly conserved and occupy relatively small sections of the Wnt sequence, the Wnt-binding regions of Fzd CRDs are distributed across several segments of the CRDs and often incorporate poorly conserved residues. Four sequences in the Fzd CRDs can be defined (Figure 6A), two of which interact with the Wnt thumb region and two of which interact with the Wnt index finger region; several additional residues of importance in specific cases (Figure S16). Highly conserved Fzd CRD residues frequently implicated in Wnt binding are generally associated with lipid binding: the FxP motif, which frequently occurs within a helix forming one side of the lipid-binding site of the Fzd CRD, and the phenylalanine of an FxW motif in the latter part of the sequence, both appear to interact with the Wnt palmitoleylation (Figure 6B). Hydrophobic residues adjacent the final cysteine in the Fzd CRD are frequently implicated in binding the Wnt index finger, as are hydrophobic residues adjacent the fourth cysteine of the Fzd CRD. However, the involvement of particular Fzd CRD residues in binding is often highly influenced by sequence variation, even for positions frequently implicated in Wnt binding. The greatest deviations in the utilization of Wnt-binding residues with respect to the set of Fzd CRDs occurs in Fzd3, Fzd6, sFRP3 and sFRP4. The region corresponding to the FxP motif in sFRP4 occurs as YEE; the tyrosine and glutamate residues in this sequence are never implicated as strong contributors to binding any Wnt. In sFRP3, the phenylalanine of the motif is retained, but the proline is replaced by glycine; the phenylalanine is strongly implicated in binding to all Wnts, while this is never the case for glycine. The glutamates of a motif frequently occurring as EAGLE are often implicated in Fzd CRD binding

to Wnt. In Fzd3 and Fzd6, the residue corresponding to the first glutamate is never strongly implicated in binding to any Wnt; this is replaced by a threonine in Fzd3 and an isoleucine in Fzd6. Substitution of this residue with aspartate (as occurs in several Fzds and sFRPs) or glutamine (as occurs in sFRP3 and sFRP4) does not appear to greatly influence the frequency with which this residue is involved in Wnt binding. Similarly, replacement of the second glutamate in the motif with alanine, as occurs in Fzd3, sFRP3 and sFRP4 eliminates the importance of this position to Wnt binding, while retaining it as a glutamate (as in Fzd6 as other Fzds and sFRPs), aspartate or even glutamine does not seem to affect the frequency of its importance to binding.

**DISCUSSION**

In this study, we have developed a model for predicting binding affinity for Wnt-Fzd interactions. Although the model was developed against a relatively small set of data from a single study, there is nonetheless excellent agreement between affinities predicted in the current study and those experimentally determined in other studies which were not included in model building and testing here. The binding affinity of Wnt3a for the mouse sFRP3 was determined by surface plasmon resonance to be 7.9nM (37); our model predicts this interaction to be at 0.28nM, suggesting strong binding affinity. Binding affinities of Wnt3a, Wnt7a, Fzd10 and sFRP4 measured using ELISA (38) confirm our model's prediction that the Fzd5-Wnt3a interaction was stronger than that of Fzd10-Wnt7a and Wnt7a-sFRP4. However, direct comparisons of $K_d$ values predicted by our model and those determined by ELISA are challenging as our model has been optimized against BLI data, where a direct interaction is measured, whereas ELISA is a coupled assay; thus, $K_d$ values obtained from BLI are likely to indicate higher affinity than those obtained from ELISA.

As experimentally determined binding affinities of Wnt-Fzd CRD interactions are largely limited to those included in our training and test sets, it is also pertinent to investigate whether interactions demonstrated experimentally through co-immunoprecipitation (coIP) were predicted by our model to have strong binding affinities. mFzd4-mWnt2b (39), hFzd4-hWnt2 (40), mFzd4-mWnt7b (41), mFzd6-Wnt4 (42) and hWnt3a-hSFRP4 (43), which were shown by coIP to interact, are predicted by our model to bind with an affinity in the intermediate or tighter range (<40nM). However, the interaction of sFRP1 with Wnt5a, which has been demonstrated by coIP (44), is suggested by our model to bind in the low micromolar range. While this would be within the range detectable by coIP, and is indeed a typical range for other interactions of biological relevance, particularly protein-carbohydrate interactions (45), binding affinities of functionally relevant Wnt-Fzd CRD interactions generally appear to occur in the low-to-mid nanomolar range, as evidenced in the data upon which we have based our prediction model. Therefore, it is likely that the affinity of the sFRP1-Wnt5a interaction is drastically underestimated by the model.

Despite the failure of the model in selected cases to achieve accurate predictions, the model nonetheless performs remarkably well at predicting binding affinities and likely interactors, particularly when considering that the Wnt-Fzd CRD interaction is rather complex due to involvement of both protein-protein and protein-lipid interactions at different sites. This would further suggest its usefulness in predicting the effect of Wnt/Fzd mutations to residues involved in either of the binding sites. The predictive success of the model is likely attributable to two main factors. The first is the use of a test set of cases separated from the training set in order to validate the model, which is not always performed in developing quantitative structure-activity relationships; even more remarkably, the use of an external data set for model validation appears to be a matter of some debate in the QSAR literature (46). The second is the incorporation of a term in the model specifically considering the contribution to binding made by the lipid. The direct involvement of Wnt lipidation in facilitating the Wnt-Fzd interaction is likely unusual among protein-protein interactions; lipidation typically appears to influence only the solubility and localization of proteins, rather than directly facilitate protein-protein interactions (47). However, other post-translational modification of proteins, such as glycosylation, phosphorylation and methylation, are very common and are often involved in facilitating protein folding and mediating protein-protein interactions (48-50). Since post-translational modifications such as these are generally not accommodated in protein-protein docking and scoring, the strategy demonstrated here is one that could be adapted to facilitate their inclusion in protein-protein docking and scoring.

This study has revealed trends with regards to the selectivity and promiscuity of Wnt

ligands for Fzd-CRDs. The study particularly highlights the promiscuous nature of sFRP4, a Wnt antagonist of interest to our group (51-56). SFRP3 is predicted to display similarly low selectivity for Wnt ligands, while SFRP1, SFRP2 and SFRP5 are predicted to display much higher selectivity. The various levels of selectivity is likely to be due to the evolutionary development of tissue expression patterns of Wnt ligands and Fzd receptors, where sFRPs can partially limit aberrant Wnt signaling in order for controlled tissue development (57).

This study has focused on the interactions of Wnt proteins with the Frizzled-type cysteine-rich domains of the Fzd receptors and the secreted Frizzled-related proteins. However, a variety of other proteins also contain Frizzled-type CRDs, albeit less closely sequence-related to those of the Fzds and sFRPs. These include Smoothened, atrial natriuretic peptide-converting enzyme (CORIN), the tyrosine-protein kinase transmembrane receptors ROR1 and ROR2, the skeletal muscle receptor tyrosine-protein kinase (MuSK) (for which a structure of the Fzd CRD has been experimentally solved (58)), the collagen XVIII α-1 chain, carboxypeptidase Z and the membrane Frizzled-related protein. With the exception of the RORs (59-62), it is unknown if any Wnt binds to these proteins, and if so, if such an interaction is functionally relevant in the context of Wnt signaling. The approaches utilized in the current study could be applied to investigate the binding of Wnts to the Frizzled-type CRDs of these proteins, which in turn, could stimulate further research into alternative Wnt signaling pathways.

It is important to note that a high affinity interaction between a given Wnt and a given CRD does not necessarily translate into a signal transduction event. Wnt signaling involves several additional proteins both extracellularly and intracellularly. For example, in canonical Wnt signaling, Wnt binds to a Fzd CRD, as well as the co-receptor LRP5/6 (63); on the intracellular side, this likely causes a conformational change in Fzd, resulting in movement of the Fzd intracellular loop 3 and C-terminal helix, which in turn, permits Dvl binding and subsequent signal transduction (64,65). Thus, the biological relevance of given Wnt-Fzd CRD interactions will be influenced by the co-expression/co-localization of these other proteins. Recent structural data on LRP6 (66-68) and the Smoothened receptor, a Class F GPCR related to Fzd receptors (69-72), as well as the availability of Dvl domain structures (73-76) and knowledge of key residues in the Fzd-Dvl interaction (64,77,78) provide the opportunity to investigate more completely the structural basis of canonical Wnt signaling. Additionally, the structures of several intracellular components in non-canonical Wnt signaling pathways are known or adopt structurally characterized folds, suggesting the potential for structural investigations. The models generated in this study provide a solid basis by which to pursue further structural studies of Wnt signaling, and perhaps of greater importance given the combinatorial nature of potential Wnt-Fzd interactions, suggest specific interacting partners on which to focus experimental and computational efforts.

## EXPERIMENTAL PROCEDURES

*Template preparation*–The template structure for all models was the complex of the *Xenopus* Wnt8 (XWnt8) with the mouse Fzd8 CRD (PDB 4F0A) (19). This structure was initially processed by the Protein Preparation Wizard, with missing side chain and loops filled in by Prime. Although the identity of the lipid modification to XWnt8 in this structure could not be conclusively determined (19), we have presumed this modification to be palmitoleic acid, as indicated either by direct experimental evidence or comparison to similar sequences for which this modification has been demonstrated (18,79-83). The lipid in the structure was manually modified using Maestro to be a palmitoleic acid modification, which involved the creation of a double bond between carbons 9 and 10, and the addition of carbons 15 and 16 to the lipid, which were missing from the structure. The lipid was subject to a Monte Carlo multiple minimum (MCMM) conformational search using Macromodel, with the region comprising carbons 9-16, as well as the hydrogen atoms attached to these carbons, defined as a freely-moving substructure, residues within 6.0 Å of this defined as a frozen shell, and a torsional constraint to ensure *cis* double bond geometry about carbons 9 and 10. Automatic setup of the substructure was employed to define rotatable bonds to be searched, however, all torsion check parameters were removed. Extended torsion sampling was employed. A maximum number of 10000 steps for the search was employed, with a maximum of 2000 steps per rotatable bond. The lowest energy structure obtained from the search provided a template structure for the lipid, used in all models.

*Homology modelling*–Sequences of Wnts, Frizzled and sFRP CRDs from both mouse and human were obtained from the UniProt database (84) (accession numbers provided in Supplemental Data, Table S1). Homology models were prepared using Prime 4.1 (85) (sequence ranges and alignments used provided in Supplemental Data, Figures S2 and S3). All models were prepared using knowledge-based building, however, due to the presence of large insertions in the human and mouse Wnt6, Wnt10a and Wnt10b sequences relative to XWnt8, an alternative strategy to building these structures was performed (*vide infra*). Disulfide bonds c13-c17 and c16-c24 in Wnt (see (36) for description of cysteine numbering in Wnts) typically could not be created during the model building process due to being adjacent to insertions/gaps in the sequence alignment; these bonds were manually inserted and the residues involved energy minimized. The lipid structure generated during template preparation was not included during Wnt model building, but manually attached following model building.

To build the structures of the human and mouse Wnt6, Wnt10a and Wnt10b, an initial model of the complete mouse Wnt10a was generated using the I-TASSER server (86). Structures of the remaining Wnts were then built using knowledge-based building in Prime against both the mouse Wnt10a model generated by I-TASSER (to provide the structure of the insertion) and the XWnt8 structure (to provide a template for modelling the remainder of the structure).

*Complex generation and refinement*–All combinations of Wnt-CRD complexes were generated by merging the structures of each of the models built in the previous step. The generated complexes were subject to refinement using Prime 4.1. The refinement process was facilitated through the use of a KNIME workflow (Figure S4). In each complex, non-template residues and residues within 6.0 Å of the binding interface were subject to Prime Minimization, Prime Side-chain Prediction, followed by a second Prime Minimization. The Wnt lipidation was excluded from the first minimization, to allow CRD residues to relax around it, but included in the second minimization. For complexes involving mouse and human Wnt6, Wnt10a and Wnt10b, the large insertions modelled by I-TASSER were also subject to the refinement procedure. The quality of the refined models was assessed using the MolProbity score, as calculated by the MolProbity module within PHENIX (87). The quality of the refined models was also assessed by calculating the root-mean-squared deviation (RMSD) of the Cα atoms and the TM-Score with respect to the XWnt8-mFzd8 CRD complex. These measurements were both calculated using MM-align (88), with the option to enforce interface alignment by the default cutoff enabled.

*Development and validation of the binding affinity prediction model*–Complexes of mouse Wnt3a, Wnt4, Wnt5a and Wnt5b with mouse Fzd1, Fzd2, Fzd4, Fzd5, Fzd7 and Fzd8 were rescored using all of the scoring functions contained in the CCharPPI server (28). As the scoring functions are generally only capable of considering interactions between protein residues, the lipid modification to Wnt was removed prior to rescoring. In order to consider contributions to the binding affinity made by the lipid, Prime MM-GB/SA calculations on the interaction between the lipid and the CRDs were performed. For these calculations, the protein component of Wnt was removed.

The scores for each complex by each scoring function in CCharPPI, as well as the values of the terms provided by the Prime MM-GB/SA calculations, were loaded into Maestro. A property containing the dissociation constants determined by BLI for selected mouse Wnt-Fzd CRD pairs (27) was manually created and used to define the activity property. Complexes involving interactions with either Wnt4 or Fzd1 comprised the test set, while all other complexes comprised the training set; the training and test sets are summarized in the Results section (Table 3). Both the training and test sets cover a diverse range of Wnts, Fzds and binding affinities for Wnt-Fzd interactions.

Strike was used to generate affinity prediction models. Multiple linear regression was used to build models. Functions from CCharPPI and properties from Prime MM-GB/SA provided the descriptors used in model building; the full list of functions and properties considered in model building is provided in Table S5 of the Supplemental Data. The success of the models in predicting binding affinities for complexes in both the training and test sets was evaluated using RMSE and the percentage of complexes for which the predicted value occurred within the experimental range ($RMSE_{train}$, $RMSE_{test}$, $InExp_{train}$, $InExp_{test}$).

All possible three-descriptor models incorporating one term from Prime MM-GB/SA and the remaining two terms from CCharPPI were

investigated. Models with $RMSE_{train}$ less than 0.5 kcal/mol and $InExp_{train}$ greater than 50% were selected for testing. Models performing at least as well for the test set for the training set (i.e., $RMSE_{test} \leq 0.5$ kcal/mol and $InExp_{test} \geq 50\%$) were selected for further elaboration into four-descriptor models, which were generated by adding an additional term from CCharPPI to the best performing three-descriptor models. Four-descriptor models giving $RMSE_{train}$ and $RMSE_{test}$ less than 0.3 kcal/mol and $InExp_{train}$ and $InExp_{test}$ greater than 75% were selected as high performing models. Elaboration of the four-descriptor models into five-descriptor models was also pursued, by adding another term from CCharPPI.

As a final check of model quality, we have also checked if the approximate range of binding affinity predicted by the best models is in that expected. Dijksterhuis et al. (27) used a simplified scheme wherein Wnt-Fzd binding affinities were classified as strong (<10nM, ++++), intermediate (10-40nM, +++), weak (40-100nM, ++), very weak (>100nM, +), and non-binding (-). We have utilized this scheme with some modification; we have considered predictions of 100-400nM to constitute the very weak (+) category, and predictions greater than 400nM to be effectively non-binding (-); the 400nM limit was chosen in relation to the intermediate/weak affinity range defined.

*Analysis of functional residues in Wnt-Fzd interactions*–All 570 Wnt-Fzd CRD models were subject to MM-GB/SA analysis using AMBER14 (35). Wnt-Fzd complexes were parameterized using the ff14SB force field (89). Parameter generation for *O*-palmitoleylserine was facilitated by *antechamber* (90), adapting procedures described in both the AMBER14 Reference Manual and AMBER tutorials. MMPBSA.py facilitated MM-GB/SA calculations (91). The modified generalized Born model of Onufriev, Bashford and Case (*igb*=5) (92) with a salt concentration of 0.1 M was used to calculate the polar desolvation energy. The non-polar desolvation energy was calculated using surface areas derived from the LCPO method (93) multiplied by surface tension (the default of 0.0072 kcal/(mol $Å^2$) was used). Energies calculated by MM-GB/SA were decomposed on a per-residue basis, with 1-4 terms added to the internal potential terms (*idecomp*=1) (94). Residues contributing greater than ±2.0 kcal/mol to the total MM-GB/SA binding energy were selected as being of functional importance to binding. Logo analysis of regions within the Wnt and Fzd sequences frequently found to contain residues of functional importance to Wnt-Fzd binding was performed using the WebLogo server (95). Sequence logos were generated as frequency plots.

**Acknowledgements:** M.A. is a recipient of a National Health and Medical Research Council CJ Martin Early Career Fellowship (GNT1054245), a Cancer Council of Western Australia Suzanne Cavanagh Early Career Investigator Grant, a Raine Priming Grant, operational research support from the Curtin Institute for Computation, and a Curtin Research Fellowship. S.P. is supported by funds from the Rotary Club of Belmont, Australian Rotary Health Research Fund and Curtin University School of Biomedical Sciences. A.D. is supported by strategic research funds from the School of Biomedical Sciences (Curtin University), Commercialisation Advisory Board of Curtin University, Cancer Council of Western Australia and Actinogen Ltd, Perth, Western Australia. The authors gratefully acknowledge Prof Yvonne Jones (University of Oxford) for critical discussion in the review of the final manuscript.

**Conflict of interest:** The authors declare that they have no conflicts of interest with the contents of this article.

**Author contributions:** MA conceived the idea for the work, conducted the experiments, analysed the results. MA and SP prepared the manuscript. MA, SP and AD critically reviewed and revised the manuscript. All authors reviewed the results and approved the final version of the manuscript.

## REFERENCES


1. Holstein, T. W. (2012) The evolution of the Wnt pathway. *Cold Spring Harb Perspect Biol* **4**, a007922
2. Hikasa, H., and Sokol, S. Y. (2013) Wnt signaling in vertebrate axis specification. *Cold Spring Harb Perspect Biol* **5**, a007955
3. Polakis, P. (2012) Wnt signaling in cancer. *Cold Spring Harb Perspect Biol* **4**, a008052
4. Komiya, Y., and Habas, R. (2008) Wnt signal transduction pathways. *Organogenesis* **4**, 68-75
5. Pohl, S. Ö.-G., Brook, N., Agostino, M., Arfuso, F., Kumar, A. P., and Dharmarajan, A. (2017) Wnt signaling in triple-negative breast cancer. *Oncogenesis* **6**, e310
6. Dijksterhuis, J. P., Petersen, J., and Schulte, G. (2014) WNT/Frizzled signalling: receptor-ligand selectivity with focus on FZD-G protein signalling and its physiological relevance: IUPHAR Review 3. *Br. J. Pharmacol.* **171**, 1195-1209
7. He, X., Semenov, M., Tamai, K., and Zeng, X. (2004) LDL receptor-related proteins 5 and 6 in Wnt/beta-catenin signaling: arrows point the way. *Development* **131**, 1663-1677
8. Wallingford, J. B., and Habas, R. (2005) The developmental biology of Dishevelled: an enigmatic protein governing cell fate and cell polarity. *Development* **132**, 4421-4436
9. Clevers, H. (2006) Wnt/beta-catenin signaling in development and disease. *Cell* **127**, 469-480
10. Huelsken, J., and Behrens, J. (2002) The Wnt signalling pathway. *J Cell Sci* **115**, 3977-3978
11. Stamos, J. L., and Weis, W. I. (2013) The beta-catenin destruction complex. *Cold Spring Harb Perspect Biol* **5**, a007898
12. Kohn, A. D., and Moon, R. T. (2005) Wnt and calcium signaling: β-catenin-independent pathways. *Cell Calcium* **38**, 439-446
13. Kühl, M., Sheldahl, L. C., Malbon, C. C., and Moon, R. T. (2000) Ca(2+)/calmodulin-dependent protein kinase II is stimulated by Wnt and Frizzled homologs and promotes ventral cell fates in Xenopus. *J Biol Chem* **275**, 12701-12711
14. Sheldahl, L. C., Park, M., Malbon, C. C., and Moon, R. T. (1999) Protein kinase C is differentially stimulated by Wnt and Frizzled homologs in a G-protein-dependent manner. *Curr Biol* **9**, 695-698
15. De, A. (2011) Wnt/Ca2+ signaling pathway: a brief overview. *Acta Biochim. Biophys. Sin.* **43**, 745-756
16. Green, J., Nusse, R., and van Amerongen, R. (2014) The role of Ryk and Ror receptor tyrosine kinases in Wnt signal transduction. *Cold Spring Harb Perspect Biol* **6**, a009175
17. Smolich, B. D., McMahon, J. A., McMahon, A. P., and Papkoff, J. (1993) Wnt family proteins are secreted and associated with the cell surface. *Mol Biol Cell* **4**, 1267-1275
18. Gao, X., and Hannoush, R. N. (2014) Single-cell imaging of Wnt palmitoylation by the acyltransferase porcupine. *Nat. Chem. Biol.* **10**, 61-68
19. Janda, C. Y., Waghray, D., Levin, A. M., Thomas, C., and Garcia, K. C. (2012) Structural basis of Wnt recognition by Frizzled. *Science* **337**, 59-64
20. Wang, Y., Macke, J. P., Abella, B. S., Andreasson, K., Worley, P., Gilbert, D. J., Copeland, N. G., Jenkins, N. A., and Nathans, J. (1996) A large family of putative transmembrane receptors homologous to the product of the Drosophila tissue polarity gene frizzled. *J Biol Chem* **271**, 4468-4476
21. Xu, Q., Wang, Y., Dabdoub, A., Smallwood, P. M., Williams, J., Woods, C., Kelley, M. W., Jiang, L., Tasman, W., Zhang, K., and Nathans, J. (2004) Vascular development in the retina and inner ear: control by Norrin and Frizzled-4, a high-affinity ligand-receptor pair. *Cell* **116**, 883-895
22. Ye, X., Wang, Y., Cahill, H., Yu, M., Badea, T. C., Smallwood, P. M., Peachey, N. S., and Nathans, J. (2009) Norrin, frizzled-4, and Lrp5 signaling in endothelial cells controls a genetic program for retinal vascularization. *Cell* **139**, 285-298

23. Surana, R., Sikka, S., Cai, W., Shin, E. M., Warrier, S. R., Tan, H. J., Arfuso, F., Fox, S. A., Dharmarajan, A. M., and Kumar, A. P. (2014) Secreted frizzled related proteins: Implications in cancers. *Biochim Biophys Acta* **1845**, 53-65
24. Cruciat, C. M., and Niehrs, C. (2013) Secreted and transmembrane wnt inhibitors and activators. *Cold Spring Harb Perspect Biol* **5**, a015081
25. Dann, C. E., Hsieh, J. C., Rattner, A., Sharma, D., Nathans, J., and Leahy, D. J. (2001) Insights into Wnt binding and signalling from the structures of two Frizzled cysteine-rich domains. *Nature* **412**, 86-90
26. Lopez-Rios, J., Esteve, P., Ruiz, J. M., and Bovolenta, P. (2008) The Netrin-related domain of Sfrp1 interacts with Wnt ligands and antagonizes their activity in the anterior neural plate. *Neural Dev* **3**, 19
27. Dijksterhuis, J. P., Baljinnyam, B., Stanger, K., Sercan, H. O., Ji, Y., Andres, O., Rubin, J. S., Hannoush, R. N., and Schulte, G. (2015) Systematic mapping of WNT-FZD protein interactions reveals functional selectivity by distinct WNT-FZD pairs. *J. Biol. Chem.* **290**, 6789-6798
28. Moal, I. H., Jiménez-García, B., and Fernandez-Recio, J. (2015) CCharPPI web server: computational characterisation of protein-protein interactions from structure. *Bioinformatics* **31**, 123-125
29. Yang, J., Yan, R., Roy, A., Xu, D., Poisson, J., and Zhang, Y. (2015) The I-TASSER Suite: protein structure and function prediction. *Nat. Methods* **12**, 7-8
30. Chen, V. B., Arendall, W. B. r., Headd, J. J., Keedy, D. A., Immormino, R. M., Kapral, G. J., Murray, L. W., Richardson, J. S., and Richardson, D. C. (2010) MolProbity: all-atom structure validation for macromolecular crystallography. *Acta Crystallogr.* **D66**, 12-21
31. Zhang, Y., and Skolnick, J. (2004) Scoring function for automated assessment of protein structure template quality. *Proteins* **57**, 702-710
32. Chaudhury, S., Lyskov, S., and Gray, J. J. (2010) PyRosetta: a script-based interface for implementing molecular modeling algorithms using Rosetta. *Bioinformatics* **26**, 689-691
33. Zhang, J., and Zhang, Y. (2010) A novel side-chain orientation dependent potential derived from random-walk reference state for protein fold selection and structure prediction. *PLoS One* **5**, e15386
34. Andrusier, N., Nussinov, R., and Wolfson, H. J. (2007) FireDock: fast interaction refinement in molecular docking. *Proteins* **69**, 139-159
35. Salomon-Ferrer, R., Case, D. A., and Walker, R. C. (2013) An overview of the Amber biomolecular simulation package. *WIREs Comput. Sci.* **3**, 198-210
36. MacDonald, B. T., Hien, A., Zhang, X., Iranloye, O., Virshup, D. M., Waterman, M. L., and He, L. (2014) Disulfide bond requirements for active Wnt ligands. *J. Biol. Chem.* **289**, 18122-18136
37. Wawrzak, D., Metioui, M., Willems, E., Hendrickx, M., de Genst, E., and Leyns, L. (2007) Wnt3a binds to several sFRPs in the nanomolar range. *Biochem. Biophys. Res. Commun.* **357**, 1119-1123
38. Carmon, K. S., and Loose, D. S. (2010) Development of a bioassay for detection of Wnt-binding affinities for individual frizzled receptors. *Anal. Biochem.* **401**, 288-294
39. Ohta, K., Ito, A., Kuriyama, S., Lupo, G., Kosaka, M., Ohnuma, S., Nakagawa, S., and Tanaka, H. (2011) Tsukushi functions as a Wnt signaling inhibitor by competing with Wnt2b for binding to transmembrane protein Frizzled4. *Proc. Natl. Acad. Sci. U. S. A.* **108**, 14962-14967
40. Klein, D., Demory, A., Peyre, F., Kroll, J., Augustin, H. G., Helfrich, W., Kzhyshkowska, J., Schledzewski, K., Arnold, B., and Goerdt, S. (2008) Wnt2 acts as a cell type-specific, autocrine growth factor in rat hepatic sinusoidal endothelial cells cross-stimulating the VEGF pathway. *Hepatology.* **47**, 1018-1031

41. Wang, Z., Shu, W., Lu, M. M., and Morrisey, E. E. (2005) Wnt7b activates canonical signaling in epithelial and vascular smooth muscle cells through interactions with Fzd1, Fzd10, and LRP5. *Mol. Cell. Biol.* **25**, 5022-5030
42. Lyons, J. P., Mueller, U. W., Ji, H., Everett, C., Fang, X., Hsieh, J. C., Barth, A. M., and McCrea, P. D. (2004) Wnt-4 activates the canonical beta-catenin-mediated Wnt pathway and binds Frizzled-6 CRD: functional implications of Wnt/beta-catenin activity in kidney epithelial cells. *Exp. Cell. Res.* **298**, 369-387
43. Constantinou, T., Baumann, F., Lacher, M. D., Saurer, S., Friis, R., and Dharmarajan, A. (2008) SFRP-4 abrogates Wnt-3a-induced beta-catenin and Akt/PKB signalling and reverses a Wnt-3a-imposed inhibition of in vitro mammary differentiation. *J. Mol. Signal.* **3**, 10
44. Matsuyama, M., Aizawa, S., and Shimono, A. (2009) Sfrp Controls Apicobasal Polarity and Oriented Cell Division in Developing Gut Epithelium. *PLoS Genetics* **5**, e1000427
45. Agostino, M., Velkov, T., Dingjan, T., Williams, S. J., Yuriev, E., and Ramsland, P. A. (2015) The carbohydrate-binding promiscuity of *Euonymus europaeus* lectin is predicted to involve a single binding site. *Glycobiology* **25**, 101-114
46. Veerasamy, R., Rajak, H., Jain, A., Sivadasan, S., Varghese, C. P., and Agrawal, R. K. (2011) Validation of QSAR models - strategies and importance. *Int. J. Drug Des. Discov.* **2**, 511-519
47. Resh, M. D. (2016) Fatty acylation of proteins: the long and the short of it. *Prog. Lipid Res.* **63**, 120-131
48. Xu, C., and Ng, D. T. W. (2015) Glycosylation-directed quality control of protein folding. *Nat Rev Mol Cell Biol* **16**, 742-752
49. Nishi, H., Hashimoto, K., and Panchenko, A. R. (2011) Phosphorylation in protein-protein binding: effect on stability and function. *Structure* **19**, 1807-1815
50. Bedford, M. T., and Clarke, S. G. (2009) Protein arginine methylation in mammals: who, what, and why. *Mol. Cell.* **33**, 1-13
51. Perumal, V., Krishnan, K., Gratton, E., Dharmarajan, A. M., and Fox, S. A. (2015) Number and brightness analysis of sFRP4 domains in live cells demonstrates vesicle association signal of the NLD domain and dynamic intracellular responses to Wnt3a. *Int. J. Biochem. Cell. Biol.* **64**, 91-96
52. Perumal, V., Pohl, S., Keane, K. N., Arfuso, F., Newsholme, P., Fox, S., and Dharmarajan, A. (2016) Therapeutic approach to target mesothelioma cancer cells using the Wnt antagonist, secreted frizzled-related protein 4: metabolic state of cancer cells. *Exp. Cell. Res.* **341**, 218-224
53. Pohl, S., Scott, R., Arfuso, F., Perumal, V., and Dharmarajan, A. (2015) Secreted frizzled-related protein 4 and its implications in cancer and apoptosis. *Tumour Biol.* **36**, 143-152
54. Warrier, S., Balu, S. K., Kumar, A. P., Millward, M., and Dharmarajan, A. (2013) Wnt antagonist, secreted frizzled-related protein 4 (sFRP4), increases chemotherapeutic response of glioma stem-like cells. *Oncol. Res.* **21**, 93-102
55. Wolf, V., Ke, G., Dharmarajan, A. M., Bielke, W., Artuso, L., Saurer, S., and Friis, R. (1997) DDC-4, an apoptosis-associated gene, is a secreted frizzled relative. *FEBS Lett.* **417**, 385-389
56. Muley, A., Majumder, S., Kolluru, G. K., Parkinson, S., Viola, H., Hool, L., Arfuso, F., Ganss, R., Dharmarajan, A., and Chatterjee, S. (2010) Secreted frizzled-related protein 4: an angiogenesis inhibitor. *Am. J. Pathol.* **176**, 1505-1516
57. Bovolenta, P., Esteve, P., Ruiz, J. M., Cisneros, E., and Lopez-Rios, J. (2008) Beyond Wnt inhibition: new functions of secreted Frizzled-related proteins in development and disease. *J. Cell. Sci.* **121**, 737-746
58. Stiegler, A. L., Burden, S. J., and Hubbard, S. R. (2009) Crystal structure of the frizzled-like cysteine-rich domain of the receptor tyrosine kinase MuSK. *J. Mol. Biol.* **393**, 1-9
59. Cui, B., Zhang, S., Chen, L., Yu, J., Widhopf, G. F., Fecteau, J.-F., Rassenti, L. Z., and Kipps, T. J. (2013) Targeting ROR1 inhibits epithelial–mesenchymal transition and metastasis. *Cancer Res.* **73**, 3649-3660

60. Henry, C., Quadir, A., Hawkins, N., Jary, E., Llamosas, E., Kumar, D., Daniels, B., Ward, R., and Ford, C. (2015) Expression of the novel Wnt receptor ROR2 is increased in breast cancer and may regulate both β-catenin dependent and independent Wnt signalling. *J. Cancer Res. Clin. Oncol.* **141**, 243-254
61. Liu, Y., Rubin, B., Bodine, P. V., and Billiard, J. (2008) Wnt5a induces homodimerization and activation of Ror2 receptor tyrosine kinase. *J Cell Biochem* **105**, 497-502
62. Zhang, S., Chen, L., Cui, B., Chuang, H. Y., Yu, J., Wang-Rodriguez, J., Tang, L., Chen, G., Basak, G. W., and Kipps, T. J. (2012) ROR1 is expressed in human breast cancer and associated with enhanced tumor-cell growth. *PLoS One* **7**, e31127
63. MacDonald, B. T., and He, X. (2012) Frizzled and LRP5/6 receptors for Wnt/β-catenin signaling. *Cold Spring Harb Perspect Biol* **4**, a007880
64. Tauriello, D. V. F., Jordens, I., Kirchner, K., Slootstra, J. W., Kruitwagen, T., Bouwman, B. A. M., Noutsou, M., Rüdiger, S. G. D., Schwamborn, K., Schambony, A., and Maurice, M. M. (2012) Wnt/b-catenin signaling requires interaction of the Dishevelled DEP domain and C terminus with a discontinuous motif in Frizzled. *Proc. Natl. Acad. Sci. U. S. A.* **109**, E812-E820
65. Cong, F., Schweizer, L., and Varmus, H. (2004) Wnt signals across the plasma membrane to activate the beta-catenin pathway by forming oligomers containing its receptors, Frizzled and LRP. *Development* **131**, 5103-5115
66. Chang, T. H., Hsieh, F. L., Zebisch, M., Harlos, K., Elegheert, J., and Jones, E. Y. (2015) Structure and functional properties of Norrin mimic Wnt for signalling with Frizzled4, Lrp5/6, and proteoglycan. *eLife* **4**, e06554
67. Cheng, Z., Biechele, T., Wei, Z., Morrone, S., Moon, R. T., Wang, L., and Xu, W. (2011) Crystal structures of the extracellular domain of LRP6 and its complex with DKK1. *Nat. Struct. Mol. Biol.* **18**, 1204-1210
68. Anh, V. E., Chu, M. L., Choi, H. J., Tran, D., Abo, A., and Weis, W. I. (2011) Structural basis of Wnt signaling inhibition by Dickkopf binding to LRP5/6. *Dev. Cell* **21**, 862-873
69. Wang, C., Wu, H., Evron, T., Vardy, E., Han, G. W., Huang, X. P., Hufeisen, S. J., Mangano, T. J., Urban, D. J., Katritch, V., Cherezov, V., Caron, M. G., Roth, B. L., and Stevens, R. C. (2014) Structural basis for smoothened receptor modulation and chemoresistance to anticancer drugs. *Nat. Commun.* **5**, 4355
70. Wang, C., Wu, H., Katritch, V., Han, G. W., Huang, X. P., Liu, W., Siu, F. Y., Roth, B. L., Cherezov, V., and Stevens, R. C. (2013) Structure of the human smoothened receptor bound to an antitumour agent. *Nature* **497**, 338-343
71. Weierstall, U., James, D., Wang, C., White, T. A., Wang, D., Liu, W., Spence, J. C., Bruce Doak, R., Nelson, G., Fromme, P., Fromme, R., Grotjohann, I., Kupitz, C., Zatsepin, N. A., Liu, H., Basu, S., Wacker, D., Han, G. W., Katritch, V., Boutet, S., Messerschmidt, M., Williams, G. J., Koglin, J. E., Marvin Siebert, M., Klinker, M., Gati, C., Shoeman, R. L., Barty, A., Chapman, H. N., Kirian, R. A., Beyerlein, K. R., Stevens, R. C., Li, D., Shah, S. T., Howe, N., Caffrey, M., and Cherezov, V. (2014) Lipidic cubic phase injector facilitates membrane protein serial femtosecond crystallography. *Nat. Commun.* **5**, 3309
72. Byrne, E. F., Sircar, R., Miller, P. S., Hedger, G., Luchetti, G., Nachtergaele, S., Tully, M. D., Mydock-McGrane, L., Covey, D. F., Rambo, R. P., Sansom, M. S., Newstead, S., Rohatgi, R., and Siebold, C. (2016) Structural basis of Smoothened regulation by its extracellular domains. *Nature* **535**, 517-522
73. Madrzak, J., Fiedler, M., Johnson, C. M., Ewan, R., Knebel, A., Bienz, M., and Chin, J. W. (2015) Ubiquitination of the Dishevelled DIX domain blocks its head-to-tail polymerization. *Nat. Commun.* **6**, 6718
74. Wong, H. C., Mao, J., Nguyen, J. T., Srinivas, S., Zhang, W., Liu, B., Li, L., Wu, D., and Zheng, J. (2000) Structural basis of the recognition of the dishevelled DEP domain in the Wnt signaling pathway. *Nat. Struct. Biol.* **7**, 1178-1184

75. Zhang, Y., Appleton, B. A., Wiesmann, C., Lau, T., Costa, M., Hannoush, R. N., and Sidhu, S. S. (2009) Inhibition of Wnt signaling by Dishevelled PDZ peptides. *Nat. Chem. Biol.* **5**, 217-219
76. Yu, A., Xing, Y., Harrison, S. C., and Kirchhausen, T. (2010) Structural analysis of the interaction between Dishevelled2 and clathrin AP-2 adaptor, a critical step in noncanonical Wnt signaling. *Structure* **18**, 1311-1320
77. Wong, H. C., Bourdelas, A., Krauss, A., Lee, H. J., Shao, Y., Wu, D., Mlodzik, M., Shi, D. L., and Zheng, J. (2003) Direct binding of the PDZ domain of Dishevelled to a conserved internal sequence in the C-terminal region of Frizzled. *Mol. Cell.* **12**, 1251-1260
78. Bertalovitz, A. C., Pau, M. S., Gao, S., Malbon, C. C., and Wang, H.-Y. (2016) Frizzled-4 C-terminus distal to KTXXXW motif is essential for normal dishevelled recruitment and Norrin-stimulated activation of Lef/Tcf-dependent transcriptional activation. *J. Mol. Signal.* **11**, 1
79. Coombs, G. S., Yu, J., Canning, C. A., Veltri, C. A., Covey, T. M., Cheong, J. K., Utomo, V., Banerjee, N., Zhang, Z. H., Jadulco, R. C., Concepcion, G. P., Bugni, T. S., Harper, M. K., Mihalek, I., Jones, C. M., Ireland, C. M., and Virshup, D. M. (2010) WLS-dependent secretion of WNT3A requires Ser209 acylation and vacuolar acidification. *J. Cell. Sci.* **123**, 3357-3367
80. Takada, R., Satomi, Y., Kurata, T., Ueno, N., Norioka, S., Kondoh, H., Takao, T., and Takada, S. (2006) Monounsaturated fatty acid modification of Wnt protein: its role in Wnt secretion. *Dev. Cell* **11**, 791-801
81. Galli, L. M., and Burrus, L. W. (2011) Differential palmit(e)oylation of Wnt 1 on C93 and S224 residues has overlapping and distinct consequences. *PLoS One* **6**, E26636
82. Doubravska, L., Krausova, M., Gradl, D., Vojtechova, M., Tumova, L., Lukas, J., Valenta, T., Pospichalova, V., Fafilek, B., Plachy, J., Sebesta, O., and Korinek, V. (2011) Fatty acid modification of Wnt1 and Wnt3a at serine is prerequisite for lipidation at cysteine and is essential for Wnt signalling. *Cell. Signal.* **23**, 837-848
83. Kakugawa, S., Langton, P. F., Zebisch, M., Howell, S. A., Chang, T. H., Liu, Y., Feizl, T., Bineva, G., O'Reilly, N., Snijders, A. P., Jones, E. Y., and Vincent, J. P. (2015) Notum deacylates Wnt proteins to suppress signalling activity. *Nature* **519**, 187-192
84. The UniProt Consortium. (2015) UniProt: a hub for protein information. *Nucleic Acids Res.* **43**, D204-D212
85. Jacobson, M. P., Friesner, R. A., Xiang, Z., and Honig, B. (2002) On the role of the crystal environment in determining protein side-chain conformations. *J. Mol. Biol.* **320**, 597-608
86. Roy, A., Kucukural, A., and Zhang, Y. (2010) I-TASSER: a unified platform for automated protein structure and function prediction. *Nature Protocols* **5**, 725-738
87. Adams, P. D., Afonine, P. V., Bunkóczi, G., Chen, V. B., Davis, I. W., Echols, N., Headd, J. J., Hung, L.-W., Kapral, G. J., Grosse-Kunstleve, A. J., McCoy, A. J., Moriarty, N. W., Oeffner, R., Read, R. J., Richardson, D. C., Richardson, J. S., Terwilliger, T. C., and Zwart, P. H. (2010) PHENIX: a comprehensive Python-based system for macromolecular structure solution. *Acta Crystallogr.* **D66**, 213-221
88. Mukherjee, S., and Zhang, Y. (2009) MM-align: a quick algorithm for aligning multiple-chain protein complex structures using iterative dynamic programming. *Nucleic Acids Res.* **37**, e83
89. Maier, J. A., Martinez, C., Kasavajhala, K., Wickstrom, L., and Hauser, K. E. S., C. (2015) ff14SB: improving the accuracy of protein side chain and backbone parameters from ff99SB. *J. Chem. Theory Comput.* **11**, 3696-3713
90. Wang, J., Wang, W., Kollman, P. A., and Case, D. A. (2006) Automatic atom type and bond type perception in molecular mechanical calculations. *J. Mol. Graph. Model.* **25**, 247-260
91. Miller, B. R. r., McGee, T. D. J., Swails, J. M., Homeyer, N., Gohlke, H., and Roitberg, A. E. (2012) *MMPBSA.py*: an efficient program for end-state free energy calculations. *J. Chem. Theory Comput.* **8**, 3314-3321
92. Onufriev, A., Bashford, D., and Case, D. A. (2004) Exploring protein native states and large-scale conformational changes with a modified generalized Born model. *Proteins* **55**, 383-394

93. Weiser, J., Shenkin, P. S., and Still, W. C. (1999) Approximate atomic surfaces from linear combinations of pairwise overlaps (LCPO). *J. Comput. Chem.* **20**, 217-230
94. Gohlke, H., Kiel, C., and Case, D. A. (2003) Insights into protein-protein binding by binding free energy calculation and free energy decomposition for the Ras-Raf and Ras-RalGDS complexes. *J. Mol. Biol.* **330**, 891-913
95. Crooks, G. E., Hon, G., Chandonia, J. M., and Brenner, S. E. (2004) WebLogo: a sequence logo generator. *Genome Res.* **14**, 1188-1190

**TABLES**

Table 1. Summary of model quality metrics.

| | **XWnt8:mFzd8 CRD complex** | **Mouse models[b]** | **Human models[b]** |
|---|---|---|---|
| **MolProbity Score** | 1.72 | 2.13 ± 0.46 | 2.08 ± 0.42 |
| **TM-Score[a]** | 1.00 | 0.91 ± 0.04 | 0.91 ± 0.05 |
| **Cα RMSD[a]** | 0.00 Å | 1.39 ± 0.39 Å | 1.39 ± 0.45 Å |

[a]TM-Score and Cα RMSDs calculated with respect to the XWnt8:mFzd8 CRD complex (PDB 4F0A). By definition, the TM-Score for an optimally overlaid structure compared to itself is one; the RMSD for an optimally overlaid structure compared to itself is zero. [b]Mean values ± two standard deviations shown; data for individual complexes shown in Supplemental Data (Tables S5-S10).

Table 2. Best performing four-descriptor models predicting Wnt-Fzd CRD binding energy.

| **Number** | **Model** | $RMSE_{train}$ (kcal/mol) | $RMSE_{test}$ (kcal/mol) | $InExp_{train}$ | $InExp_{test}$ |
|---|---|---|---|---|---|
| 1 | $\Delta G = 0.0038165 \times$ AP_calRW – $0.22506 \times$ MMGBSA dG Bind vdW – $0.24626 \times$ HBOND2 – $0.049875 \times$ FIREDOCK_AB – 3.3475 | 0.23 | 0.27 | 80% | 75% |
| 2 | $\Delta G = 0.0021829 \times$ AP_calRWp – $0.22111 \times$ MMGBSA dG Bind vdW – $0.20861 \times$ HBOND2 – $0.08699 \times$ ROSETTADOCK – 7.7974 | 0.30 | 0.23 | 73% | 75% |

Table 3. Comparison of predictions by Model 1 to experimental data for the training and test sets.[a]

| Interaction | $\Delta G_{Exp}$[b] | $\Delta G_{Pred}$[b] | $\lvert\Delta G_{Exp} - \Delta G_{Pred}\rvert$[b,c] | Experimental $K_d$[a] | Predicted $K_d$[a] | Experimental range (predicted range)[d] | Set |
|---|---|---|---|---|---|---|---|
| mWnt3a-mFzd2 | -10.64 | -11.16 | 0.52 | 15.7 | 6.5 | +++ (++++) | Training |
| mWnt3a-mFzd4 | -11.27 | -11.21 | 0.06 | 5.4 | 6.0 | ++++ (++++) | Training |
| mWnt3a-mFzd5 | -11.60 | -11.65 | 0.05 | 3.1 | 2.9 | ++++ (++++) | Training |
| mWnt3a-mFzd7 | -11.28 | -10.85 | 0.43 | 5.3 | 11.0 | ++++ (+++) | Training |
| mWnt3a-mFzd8 | -12.03 | -11.86 | 0.17 | 1.5 | 2.0 | ++++ (++++) | Training |
| mWnt5-mFzd2 | -10.38 | -10.33 | 0.05 | 24.4 | 26.5 | +++ (+++) | Training |
| mWnt5-mFzd4 | -10.38 | -10.26 | 0.12 | 24.4 | 29.9 | +++ (+++) | Training |
| mWnt5-mFzd5 | -11.31 | -11.19 | 0.12 | 5.1 | 6.2 | ++++ (++++) | Training |
| mWnt5-mFzd7 | -10.05 | -9.98 | 0.07 | 42.6 | 47.9 | ++ (++) | Training |
| mWnt5-mFzd8 | -11.45 | -11.43 | 0.02 | 4.0 | 4.1 | ++++ (++++) | Training |
| mWnt5b-mFzd2 | -9.60 | -9.47 | 0.13 | 91.0 | 113.4 | ++ (+) | Training |
| mWnt5b-mFzd4 | -9.95 | -10.29 | 0.34 | 50.4 | 28.4 | ++ (+++) | Training |
| mWnt5b-mFzd5 | -10.44 | -10.35 | 0.09 | 22.0 | 25.7 | +++ (+++) | Training |
| mWnt5b-mFzd7 | -9.65 | -9.89 | 0.24 | 83.7 | 55.8 | ++ (++) | Training |
| mWnt5b-mFzd8 | -11.04 | -11.19 | 0.15 | 8.0 | 6.2 | ++++ (++++) | Training |
| mWnt3a-mFzd1 | -10.66 | -10.61 | 0.05 | 15.2 | 16.5 | ++++ (++++) | Test |
| mWnt4-mFzd2 | -9.53 | -9.53 | 0.00 | 102.5 | 102.5 | + (+) | Test |
| mWnt4-mFzd4 | -10.04 | -9.72 | 0.32 | 43.3 | 74.3 | ++ (++) | Test |
| mWnt4-mFzd5 | -10.68 | -11.25 | 0.57 | 14.7 | 5.6 | +++ (++++) | Test |
| mWnt4-mFzd7 | -9.58 | -9.83 | 0.25 | 94.2 | 61.7 | + (+) | Test |
| mWnt4-mFzd8 | -10.95 | -10.70 | 0.25 | 9.3 | 14.2 | ++++ (+++) | Test |
| mWnt5-mFzd1 | -10.33 | -10.31 | 0.02 | 26.5 | 27.4 | +++ (+++) | Test |
| mWnt5b-mFzd1 | -9.60 | -9.85 | 0.25 | 91.0 | 59.7 | + (+) | Test |

[a]$K_d$ values were obtained from Dijksterhuis et al. (27) and represent the average values reported. All $K_d$ values expressed in nM. [b]$\Delta G_{exp}$ calculated from experimental $K_d$ values as $\Delta G = RT \ln K_d$, where R is

the gas constant ($1.987 \times 10^{-3}$ kcal $K^{-1}$ $mol^{-1}$) and T is the temperature at standard conditions (298K). Predicted ΔG ($\Delta G_{pred}$) calculated according to Model 1. ΔG values expressed as kcal/mol. [c]Absolute value of difference between experimental and predicted ΔG values. [d]Guide to affinity range classifications: <10nM – ++++; 10-40nM – +++; 40-100nM – ++; 100-400nM – +; >400nM – -. Cases in which the experimental and predicted $K_d$ values occur in different ranges are underlined. Range in which value of experimental $K_d$ occurs shown outside parentheses; range in which predicted $K_d$ value occurs shown inside parentheses.

**FIGURE LEGENDS**

**FIGURE 1**. Wnt signaling pathways. A. Canonical Wnt signaling. Wnt binding to Fzd-CRD initiates the destabilisation of the cytoplasmic destruction complex (APC, Axin, GSK3, CK1, Dvl). This allows cytosolic β-catenin accumulation and subsequent translocation to the nucleus where it binds to TCF/LEF transcription factors to transcribe Wnt target genes. SFRPs antagonise this cascade and β-catenin is polyubiquitinated by β-TrCP and degraded by proteolysis. B. The Wnt/Ca2+ pathway. Wnt binding to Fzd-CRD, or Ryk co-receptor activates Dvl, which stimulates calcium release. Downstream effectors PKC, CaMKII and Calcineurin (Cn) activate transcription factors CREB, NF-κB and NFAT. C. The planar cell polarity (PCP) pathway. Wnt stimulation is effected initially through Fzd-Dvl interaction and co-receptors ROR/Ryk and passed through multiple effectors downstream to ROCK and JNK. ROCK regulates the actin cytoskeleton and JNK activates AP1 and JUN transcription factors to regulate cell polarity and migration.

**FIGURE 2**. Homology models of selected Wnt-Fzd CRD complexes overlaid to the repaired XWnt8:mFzd8 CRD crystal structure (PDB 4F0A). Figure legend: grey – repaired PDB 4F0A; pink – mWnt5:mFzd1 CRD complex; yellow – mWnt10a:mFzd6 complex; green – hWnt3a:hSFRP4 CRD complex; cyan – hWnt2b:hFzd9 CRD complex. Lipid shown in all structure as sticks with transparent spheres.

**FIGURE 3.** Overview of the model building process. RMSE and InExp cutoffs used to select models at the relevant stages of model building are described in the Experimental Procedures.

**FIGURE 4**. Comparison of binding energy predictions by Model 1 in the training set (A) and test set (B). Points indicated by open squares are those where the predicted binding energy falls outside the model RMSE (0.23 kcal/mol for the training set; 0.27 kcal/mol for the test set).

**FIGURE 5**. Binding affinity predictions by Model 1 for Wnt-Fzd interactions. A. Mouse interactions. B. Human interactions. C. Binding affinity differences ($\Delta K_d$) between equivalent Wnt-Fzd interactions of mouse and human, calculated as $\Delta K_d$ = mouse $K_d$ – human $K_d$. Positive $\Delta K_d$ is indicative of a lower affinity interaction in mouse compared to human; negative $\Delta K_d$ indicates a higher affinity interaction in mouse compared to human.

**FIGURE 6.** Residues making significant contributions to the binding energy in the majority of Wnt-Fzd CRD complexes. A. Logo analyses of Wnts (first row) and Fzd CRDs (second two rows), highlighting the major regions involved in interactions. Fzd sequences interacting with a specific region of Wnt are shown below the sequence of Wnt corresponding to that region. Color guide to logos: green – aromatic residues (Trp, Phe, His, Tyr); grey – aliphatic residues (Val, Leu, Ile, Met, Ala); blue – basic residues (Arg, Lys); red – acidic residues (Asp, Glu); yellow – cysteine; light blue – palmitoleyl serine (panel A only); black – all other residues (Gly, Pro, Ser, Thr, Gln, Asn). Logos presented as frequency plots. Intensity of purple shading indicates the number of complexes in which the residue at that position is a significant contributor to the complex binding energy. B, C. Cross-eyed stereo views of the "front" (B) and rear (C) of the XWnt8-mFzd8 crystal structure complex (PDB 4F0A), with major interacting regions highlighted. Residues corresponding to positions frequently involved in interactions across the full set of Wnt-Fzd CRD complexes are shown as sticks. Regions are colored according to the caption color in Figure 5A. The "front" view displays the regions of the middle row of Figure 5A; the "rear" view displays the regions of the bottom row of Figure 5A.

**FIGURE 1**

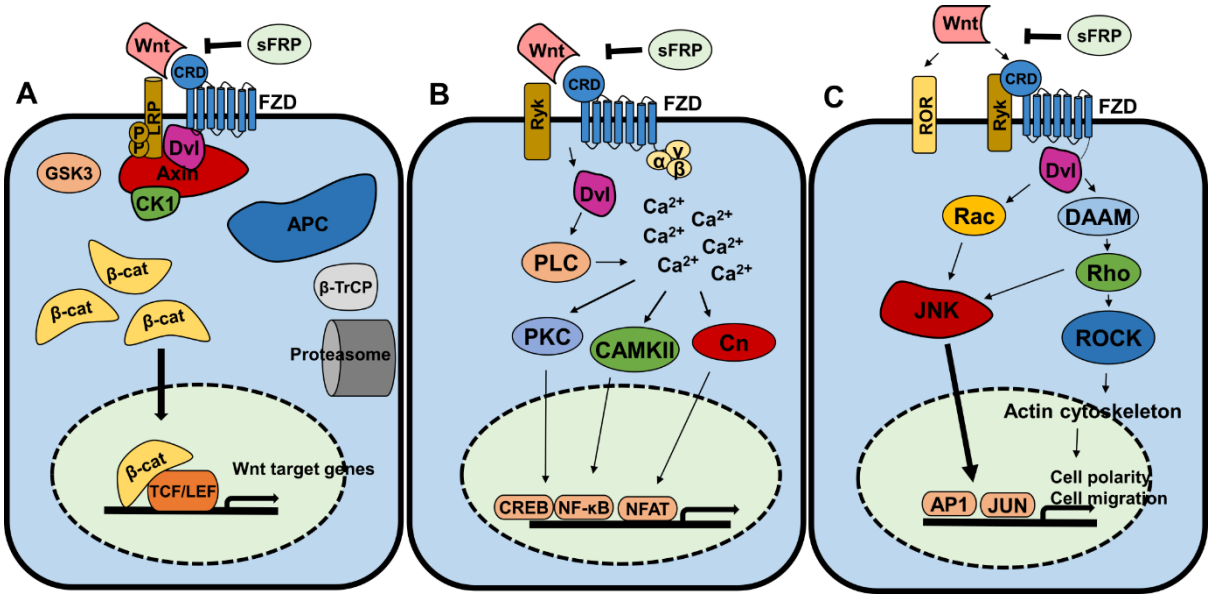
A
Wnt
sFRP
CRD
FZD
LRP
P
P
Dvl
GSK3
Axin
CK1
APC
β-cat
β-cat
β-cat
β-TrCP
Proteasome
β-cat
TCF/LEF
Wnt target genes
B
Wnt
sFRP
CRD
Ryk
FZD
α
γ
β
Dvl
Ca2+
Ca2+
Ca2+
Ca2+
Ca2+
Ca2+
PLC
PKC
CAMKII
Cn
CREB
NF-κB
NFAT
C
Wnt
sFRP
ROR
CRD
Ryk
FZD
Dvl
Rac
DAAM
Rho
JNK
ROCK
Actin cytoskeleton
Cell polarity
Cell migration
AP1
JUN

**FIGURE 2**

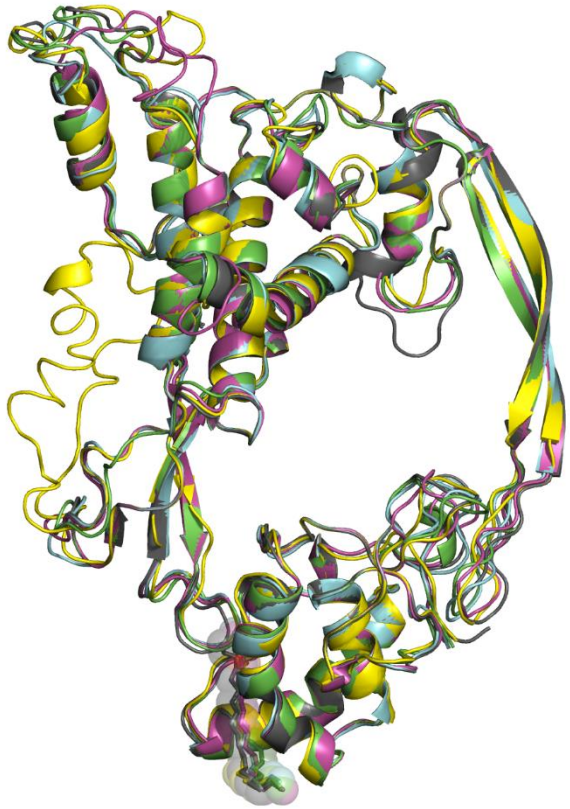

**FIGURE 3**

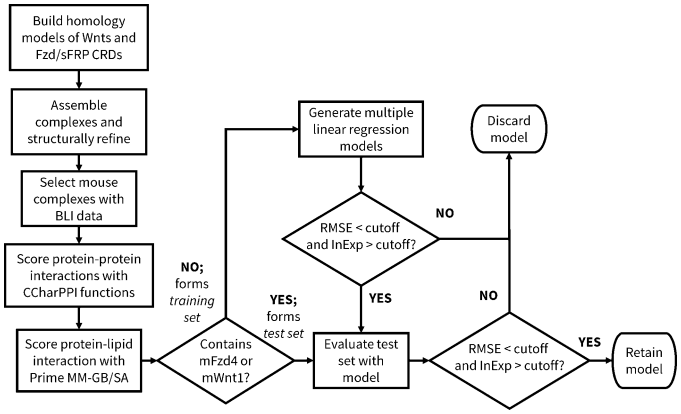
Build homology models of Wnts and Fzd/sFRP CRDs
Assemble complexes and structurally refine
Select mouse complexes with BLI data
Score protein-protein interactions with CCharPPI functions
Score protein-lipid interaction with Prime MM-GB/SA
Contains mFzd4 or mWnt1?
NO; forms training set
YES; forms test set
Generate multiple linear regression models
RMSE < cutoff and InExp > cutoff?
NO
YES
Discard model
Evaluate test set with model
RMSE < cutoff and InExp > cutoff?
NO
YES
Retain model

**FIGURE 4**

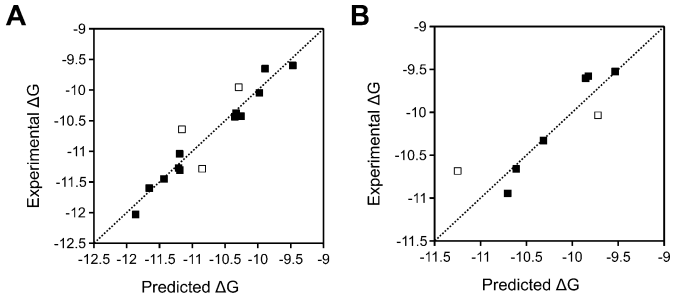
A
Experimental ΔG
Predicted ΔG
-9
-9.5
-10
-10.5
-11
-11.5
-12
-12.5
B
Experimental ΔG
Predicted ΔG
-9
-9.5
-10
-10.5
-11
-11.5

**FIGURE 5**

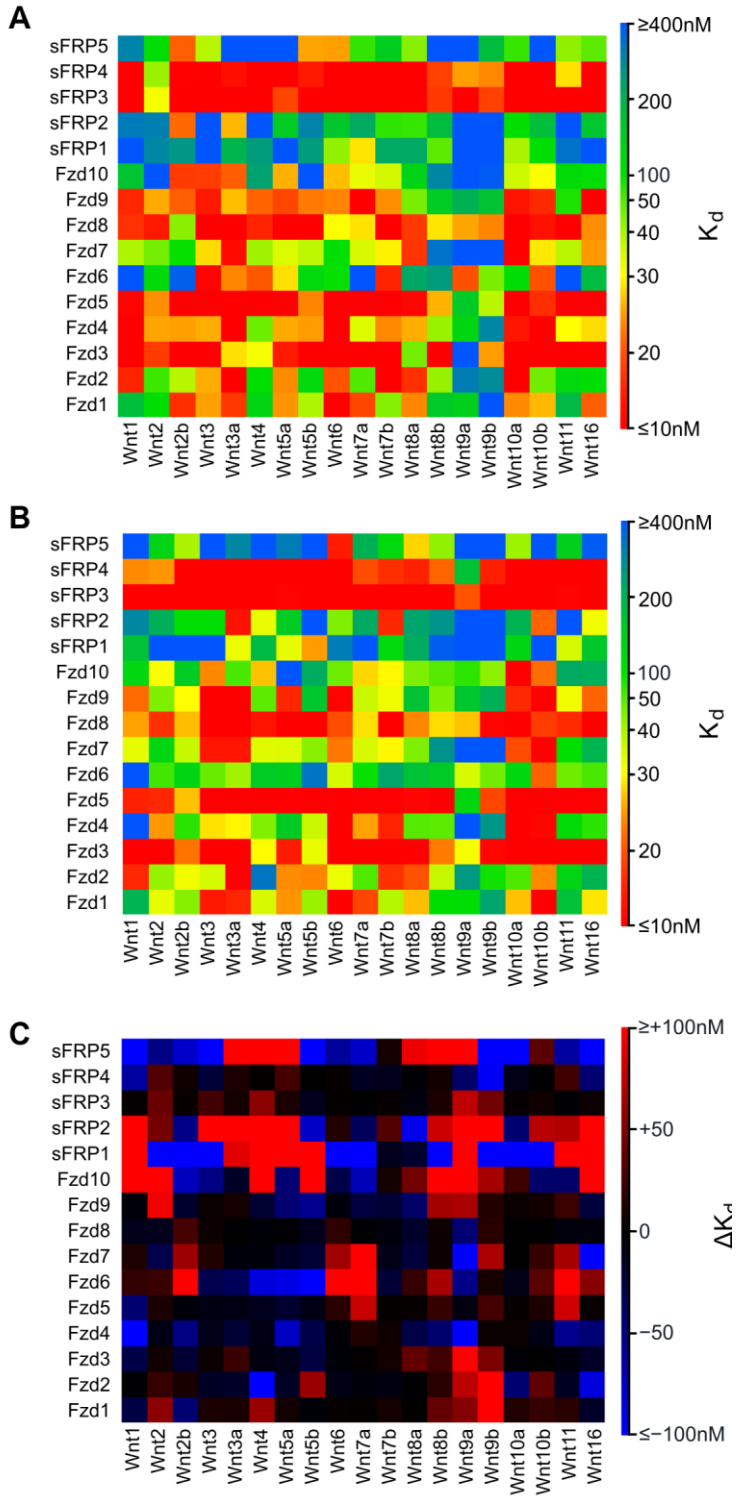
A
sFRP5
sFRP4
sFRP3
sFRP2
sFRP1
Fzd10
Fzd9
Fzd8
Fzd7
Fzd6
Fzd5
Fzd4
Fzd3
Fzd2
Fzd1
Wnt1 Wnt2 Wnt2b Wnt3 Wnt3a Wnt4 Wnt5a Wnt5b Wnt6 Wnt7a Wnt7b Wnt8a Wnt8b Wnt9a Wnt9b Wnt10a Wnt10b Wnt11 Wnt16
≥400nM
200
100
50
40
30
20
≤10nM
Kd
B
sFRP5
sFRP4
sFRP3
sFRP2
sFRP1
Fzd10
Fzd9
Fzd8
Fzd7
Fzd6
Fzd5
Fzd4
Fzd3
Fzd2
Fzd1
Wnt1 Wnt2 Wnt2b Wnt3 Wnt3a Wnt4 Wnt5a Wnt5b Wnt6 Wnt7a Wnt7b Wnt8a Wnt8b Wnt9a Wnt9b Wnt10a Wnt10b Wnt11 Wnt16
≥400nM
200
100
50
40
30
20
≤10nM
Kd
C
sFRP5
sFRP4
sFRP3
sFRP2
sFRP1
Fzd10
Fzd9
Fzd8
Fzd7
Fzd6
Fzd5
Fzd4
Fzd3
Fzd2
Fzd1
Wnt1 Wnt2 Wnt2b Wnt3 Wnt3a Wnt4 Wnt5a Wnt5b Wnt6 Wnt7a Wnt7b Wnt8a Wnt8b Wnt9a Wnt9b Wnt10a Wnt10b Wnt11 Wnt16
≥+100nM
+50
0
−50
≤−100nM
ΔKd

**FIGURE 6**

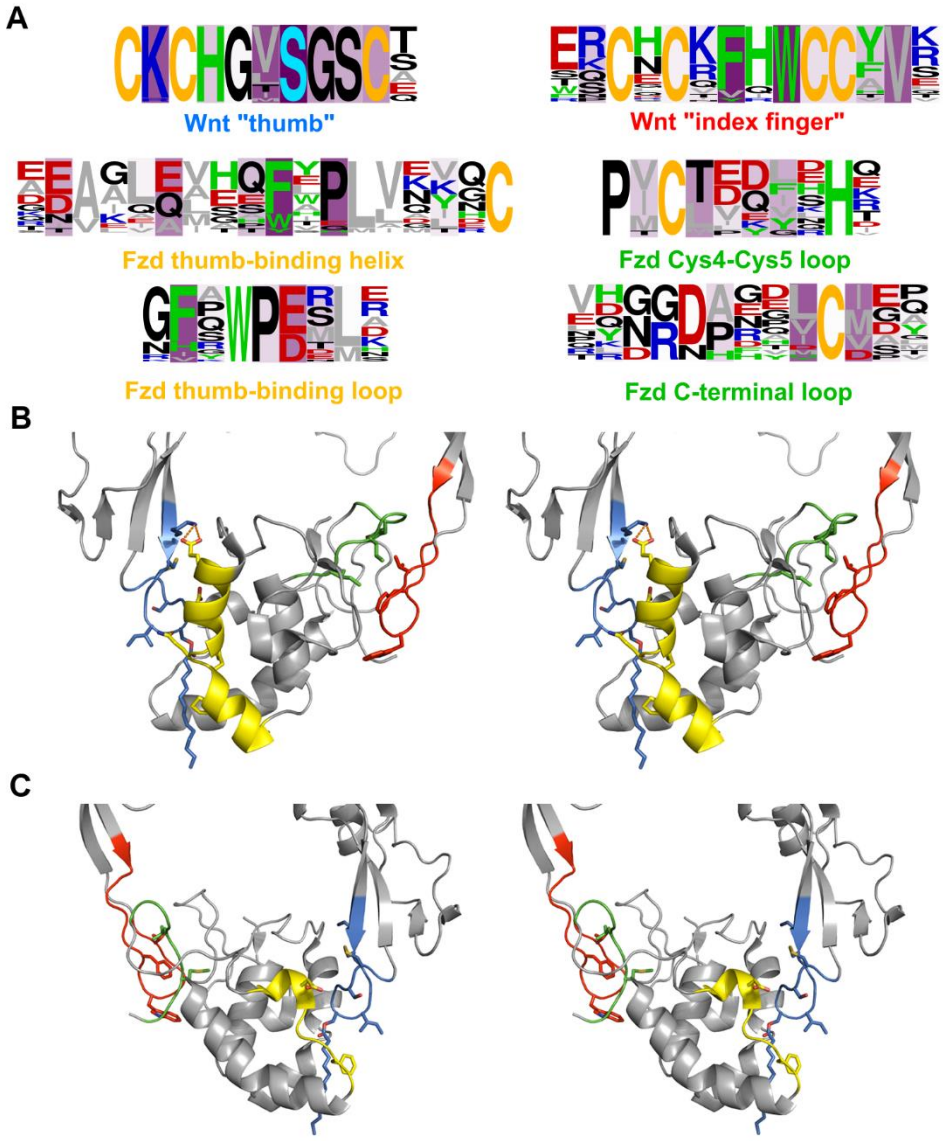
A
Wnt "thumb"
Wnt "index finger"
Fzd thumb-binding helix
Fzd Cys4-Cys5 loop
Fzd thumb-binding loop
Fzd C-terminal loop
B
C